

Article

Study on Efficient and Stable Energy Conversion Method of Oscillating Water Column Device Based on Energy Storage Valve Control

Yunpeng Hai ^{1,2}, Zhenyu Yuan ³, Changdong Wei ³, Yanjun Liu ^{1,2,3,*}  and Gang Xue ^{1,2,3,*} 

¹ Key Laboratory of High-Efficiency and Clean Mechanical Manufacture of Ministry of Education, Shandong University, Jinan 250061, China; alfred_hye@163.com

² School of Mechanical Engineering, Shandong University, Jinan 250061, China

³ Institute of Marine Science and Technology, Shandong University, Qingdao 266237, China; y1441588636@163.com (Z.Y.); wcd1220@mail.sdu.edu.cn (C.W.)

* Correspondence: lyj111yjslw@163.com (Y.L.); xuegangzb@163.com (G.X.)

Abstract: Despite extensive research on the performance of Oscillating Water Columns (OWC) over the years, issues with low energy conversion efficiency and unstable power generation have not been addressed. In this study, a novel OWC energy conversion system is proposed based on the working principle of energy storage valve control. The system utilizes accumulators and valve groups to enhance the stability of energy conversion. The hydrodynamic model of the OWC system and the pneumatic model of the novel power take-off (PTO) system are developed using numerical simulations. Building on this, the impact of the incident wave period, wave height, and air chamber opening ratio on the system's total hydrodynamic performance are examined. The results from the hydrodynamic analysis are subsequently used as input conditions to evaluate the proposed PTO system's performance. The results show that the hydrodynamic efficiency of the system presents a tendency to increase and then decrease with the increase in the incident wave period, and an optimal period exists. The air chamber opening ratio has a notable influence on the hydrodynamic characteristics of the OWC system, and the larger system damping could be set to achieve a higher capture efficiency in the low-frequency water environment. The incident wave height has a lesser effect on the hydrodynamic characteristics and the resonant period of the device. The designed novel PTO system can effectively improve the energy conversion stability of the OWC device, the flow volatility through the turbine can be reduced by 53.49%, and the output power volatility can be reduced by 25.46% compared with the conventional PTO system.

Keywords: OWC; hydrodynamic performance; accumulator; numerical simulation



Academic Editor: Andrea Frazzica

Received: 8 January 2025

Revised: 26 January 2025

Accepted: 28 January 2025

Published: 31 January 2025

Citation: Hai, Y.; Yuan, Z.; Wei, C.; Liu, Y.; Xue, G. Study on Efficient and Stable Energy Conversion Method of Oscillating Water Column Device Based on Energy Storage Valve Control. *Energies* **2025**, *18*, 666. <https://doi.org/10.3390/en18030666>

Copyright: © 2025 by the authors. Licensee MDPI, Basel, Switzerland. This article is an open access article distributed under the terms and conditions of the Creative Commons Attribution (CC BY) license (<https://creativecommons.org/licenses/by/4.0/>).

1. Introduction

Recent years have witnessed a gradual increase in the research and utilization of marine renewable energy, driven by growing environmental concerns and the declining reserves of fossil fuels. Compared with fossil fuels, marine energy is characterized by zero emissions and no pollution, so it has huge development potential and application value [1]. Among the types of marine energy, wave energy, which has energy density and high availability, has also received more and more attention [2].

Wave energy converters (WEC) have been developed in thousands of models, which can be divided into three categories according to the different ways of obtaining energy,

namely Overtopping, oscillating bodies, and Oscillating Water Columns [3]. Overtopping devices mainly use waterways to introduce waves into high-water reservoirs to form a water level difference. The stored water is gradually released to drive hydraulic turbines, converting the potential energy of water into other energy. While the energy output is more stable, the device is often required to be large in size, impacting the marine environment [4] and incurring high construction and maintenance costs. Oscillatory body systems, also known as wave-activated body systems, are based on the interaction of an object with a wave, which causes the object to oscillate and converts it into other forms of energy using a power output mechanism [5]. Most oscillating body systems use a lift and pitch mechanism. The energy conversion efficiency is relatively high, and the single body occupies a small area with little influence on the wave field. The form is flexible and can be arranged according to the local wave conditions. However, the large number and complexity of the structural components make it challenging to design and maintain [6]. The direct contact between the device and the waves affects its long-term reliability, and the overall risk of damage is high. OWC devices are significantly affected by wave frequency and amplitude, and although the overall conversion efficiency is low, compared to other WEC, the OWC device offers several distinct advantages: their mechanical components and structure are relatively simple [7], they can work effectively even under low-frequency wave settings, generally below 0.1 Hz [8], while the compressibility of the air within the chamber acts like a spring, effectively reducing structural stresses [9]. As a result, OWC devices have been widely studied and used. The research and development of OWC devices date back to the 1940s [10] when they were initially integrated into navigation buoys. In the 1970s, higher power OWCs were installed on floating barges to provide them with some electrical power [11].

So far, OWC has been investigated by numerous scholars, who mainly use three basic methods: analytical derivation, physical modeling experiments and numerical simulation. Delauré et al. [7] used the boundary element method (BEM) to solve the diffraction and radiation potential problems associated with a three-dimensional OWC device. Evans et al. [8] modeled a two-dimensional thin-walled OWC primarily in the frequency domain, with derived formulas concerning scattering and radiation issues. Josset et al. [12] developed a time-domain model for a stationary OWC using the linear boundary element method, which was then utilized to predict and analyze the annual power generation of the OWC on Pico Island. Nagata et al. [13] investigated a two-dimensional floating OWC in the frequency domain using the boundary element method with linear thermodynamics, accounting for variations in air temperature and density, as well as dynamic pressure, on the internal surface of the air chamber. Iturrioz et al. [14] developed a time-domain numerical model of a floating OWC based on the linear wave theory, and also carried out numerical modeling simulations and physical modeling experiments to validate the accuracy of the proposed model. Mavrakos et al. [15] performed a comprehensive solution for a floating vertical axisymmetric OWC device using an analytical method, analyzing and evaluating key factors, such as the hydrodynamic parameters and the mean second-order wave drift forces. Ning et al. [16] developed a novel cylindrical OWC WEC with dual chambers based on linear potential flow theory and the eigenfunction expansion technique, designed to harness wave energy from deep-water waves. Ning et al. [17] mathematically modeled a dual-chamber OWC WEC featuring a common orifice and the time-domain higher-order boundary element method, and employing potential flow theory. Konispoliatis et al. [18] performed a geometrical analysis of single-chamber versus dual-chamber WECs based on the linear potential flow theory with respect to parameters such as the wall thickness and draught of the chambers. The investigation demonstrated that the dual-chamber OWCs displayed improved hydrodynamic performance at particular wave numbers. The

above studies show that the structural parameters and configurations significantly impact the overall energy conversion efficiency of OWC, which provides a theoretical basis for further studies. However, analytical derivation is often based on idealized conditions and simplified assumptions, and there is a limited body of research addressing complex wave conditions, nonlinearities, and viscosities in waves.

For this reason, the experimental physical modeling approach has been indispensable in developing OWC devices, and many previous scholars have done much work on it. Ning et al. [19] examined the impact of incident wave conditions, such as the device width, front wall draft depth, and bottom slope on the hydrodynamic performance of fixed OWC devices via a comprehensive series of physical experiments. Ning et al. [20] further performed experimental studies on the hydrodynamic efficiency of a terrestrial dual-chamber OWC system, finding that both peak efficiency and effective frequency bandwidth were improved, enhancing its application prospects. Lopez et al. [21] carried out modeling tests and compared them with simulations to investigate the effect of air compressibility and concluded that ignoring air compressibility leads to inaccurate estimates of the resonant period and capture width ratio, but the effect is relatively small, and this effect is acceptable during the initial stages of the design. Liu et al. [22] utilized a turbomachine model to replace the orifice plate used in the mainstream of previous model tests, investigating the conversion efficiencies of the two conversion stages. Zhou et al. [23] investigated the impact of moorings on OWC devices and found through physical experiments that the dimensionless amplitudes of air chamber pressure and mean air chamber level height exhibit similar trends with wave steepness. Additionally, both effective frequency bandwidth and hydrodynamic efficiency augment with increased mooring stiffness. Joensen et al. [24] investigated the energy capture of OWC in both phases and the effect of using check valves on the overall device by adding passive check valves to the model. However, physical model experiments are relatively costly, involving significant expenses for equipment procurement, model fabrication, and ongoing maintenance. Conducting a series of experiments also requires substantial human and material resources.

In recent years, with the continuous development of computer technology [25], research on viscous flow models in fluid dynamics can also be further developed rapidly, and more people have gradually begun to use Computational Fluid Dynamics (CFD) simulations [26] to carry out OWC-related research. CFD-based numerical models inherently account for fluid viscosity compared to potential flow models [27]. Liu et al. [28] used Fluent to simulate and predict the overall energy conversion of the OWC as a whole from the wave to the final power generation and predicted the overall performance of the actual device. Yang et al. [29] used STAR-CCM+ (Version: 2019.3.1) to simulate and analyze a hybrid OWC system combined with a heaving floater WEC, and investigated the effects of the inlet height and air chamber ratio on the device's energy harvesting power, finding that the combined structure can effectively improve the efficiency of wave dissipation of the breakwater. Zeng et al. [30] conducted numerical simulations of a circular bottom-sitting OWC wave energy device using STAR-CCM+ software, and found that the SST $k-\omega$ turbulence model was more suitable for OWC numerical simulations by comparing it with experimental data. Fan et al. [31] used Fluent and restricted the degrees of freedom of the device, except for the heave, to investigate the effects of static and heave motions, as well as the opening ratio, on the efficiency of OWC energy conversion. Peng et al. [32] used Ansys Fluent 19 to study the hysteresis characteristics produced by the turbine on the OWC and found that the compressibility of the air contributes to the turbine's hysteresis effect. Xie et al. [33] developed a fast-computing numerical model for the OWC using OpenFOAM., which improved the simulation speed by 10 times over the traditional model, and examined how row and column spacing affect array gain in an OWC system. The

numerical simulation method effectively captures complex wave phenomena, including wave breaking, eddy currents, and turbulence, thereby improving the accuracy of the results. Additionally, it offers a more flexible and cost-effective approach for simulating complex physical processes under controlled conditions.

In summary, the previous research focused on the hydrodynamic energy conversion mechanism of OWC devices. Researchers sought to determine the optimal device configurations for different sea conditions and analyzed the effects of various structural and wave parameters on the device's energy conversion using diverse research methods. However, due to the inherent characteristics of waves and the operating principles of OWC devices, energy capture stability remains relatively low. Despite its significance, there are limited domestic and international studies that specifically address improving energy capture stability in such systems. Therefore, a new power take-off system is designed in this paper to improve the overall stability of the OWC device.

The following portions of the paper are structured as outlined below: Section 2 elucidates the power generation principle of the OWC and the system design of the novel PTO. The construction of the numerical model and the verification of the modeling accuracy are presented in Section 3. In Section 4, the energy conversion process of the OWC is investigated, and the effects of different incidence periods, wave heights, and opening ratios on the hydrodynamic characteristics of the device are discussed. In Section 5, the operating characteristics of the novel PTO system are investigated, and the effects of the accumulator device on the energy conversion stability are analyzed. Finally, a conclusion is given in Section 6.

2. System Power Generation Principle

The structure of the OWC device is shown in Figure 1, which mainly consists of two parts: an air chamber structure with openings at the bottom of the submerged water and a PTO system mounted at the top of the air chamber for energy conversion. The incident wave vibrates the water column up and down inside the chamber, forcing the airflow to reciprocate. The airflow, which varies with the wave cycle, rotates the turbine, and a generator connected to the turbine converts the mechanical energy of the turbine rotation into electrical energy.

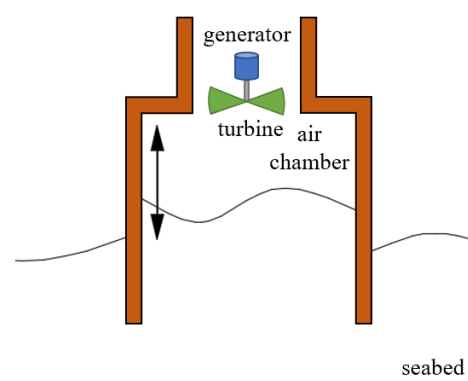


Figure 1. Diagram of the OWC apparatus.

According to the above working principle, which can be found in a wave cycle, the water column inside the air chamber fluctuates up and down, causing the air within the chamber to compress and expand so that the air pressure changes between positive and negative pressure. When the gas chamber transitions from positive pressure to negative pressure or vice versa, there will be a moment when the air pressure inside the chamber equals the outside atmosphere. At this time, the pressure difference is zero, the gas will

not go in and out of the chamber, and so cannot drive the turbine to work. Moreover, under actual sea conditions where waves vary irregularly, the air flux and pneumatic pressure flowing through the turbine change frequently. Under the transient impact of the reciprocating airflow, it is difficult to maintain a relatively constant rotational speed of the turbine, resulting in a significant fluctuation in power generated. Ultimately, the quality of the power supplied to the system declines, significantly complicating eventual grid integration [34]. Most of the turbines in PTO systems use self-rectifying turbines, which can rotate unidirectionally in both airflow directions. Moreover, unidirectional turbines have been tested across different OWC installations, such as the twin turbines [35], the SeaBreath [36], and the Tupperwave [37].

In this paper, a novel PTO system based on the working principle of energy storage valve control is designed. The system utilizes accumulators and switching valves to make the airflow produce smooth and continuous excitation to the turbine. It also utilizes check valves to form a rectification circuit, replacing the self-rectifying turbine with a unidirectional turbine to realize smooth energy conversion. The structure of the overall novel PTO system is shown in Figure 2, and the OWC air chamber is connected to the PTO system through piping.

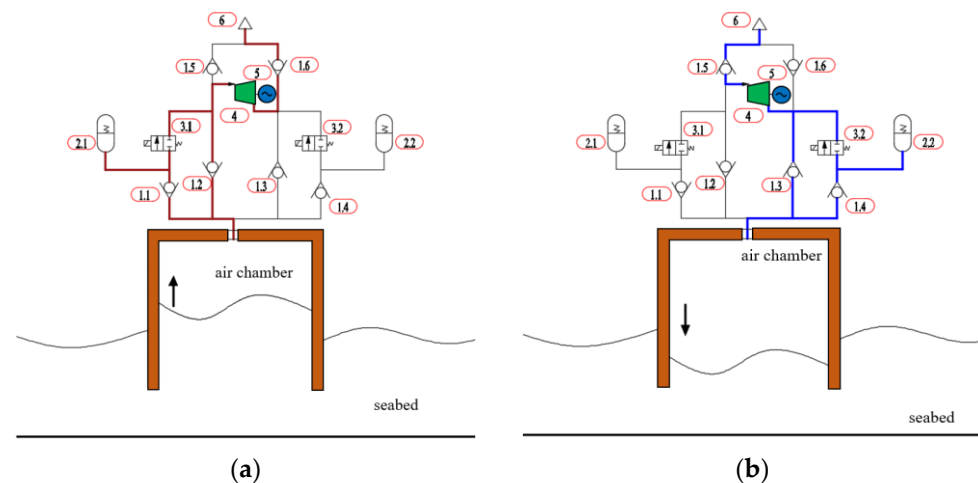


Figure 2. Schematic of the novel PTO system: (a) wave rising phase and (b) wave falling phase. 1.1–1.6: Check valves; 2.1, 2.2: accumulators; 3.1, 3.2: switching valves; 4: turbine; 5: generator; and 6: atmosphere.

When the wave inside the air chamber rises, the air pressure becomes higher than the atmospheric pressure. The airflow inflates accumulator 2.1 through check valve 1.1 and drives the turbine through check valve 1.2.

The air pressure sensor is used to detect the air chamber pressure; when the pressure is lower than the set value, this indicates that the air chamber pressure is already low and the airflow through the turbine is decreasing. At this time, the control switch valve 3.1 opens, and the accumulator 2.1 releases energy to further drive the rotation of the turbine. The airflow passes through the turbine and check valve 1.6 before exiting the system into the atmosphere.

When the wave inside the air chamber falls, the pressure decreases and becomes lower than the atmospheric pressure, thereby forming negative pressure. Consequently, the air in the atmosphere flows into the system through check valve 1.5 and drives the rotation of the turbine. Thereafter, the airflow enters the air chamber through check valve 1.3. Concurrently, the decline in pressure within the air chamber prompts airflow from accumulator 2.2 into the air chamber through check valve 1.4. This process reduces the

volume of the storage chamber within accumulator 2.2 and causes a consequent decrease in air pressure.

If the air pressure sensor detects air chamber pressure that exceeds the preset value, it indicates an imminent equilibrium between the air chamber pressure and outside pressure. Consequently, the airflow through the turbine is reduced. Concurrently, switching valve 3.2 is opened, thereby establishing a new negative pressure chamber through accumulator 2.2 and maintaining the turbine's operation.

3. Hydrodynamic Numerical Analysis Model

In this paper, the hydrodynamic performance of the device is mainly studied by numerical simulation. The CFD software STAR-CCM+ (Version: 2410.1) is employed to simulate wave conditions more realistically. The wave power absorbed by the air chamber component of the device under varying incident wave conditions is calculated in the time domain to investigate the optimal capture effect of the device.

3.1. Experimental Modeling

The primary structure of the OWC air chamber adopts a cylindrical configuration. A full-size model with $R_{full} = 5$ m, $D_{full} = 0.1$ m, $d_{full} = 2$ m was designed, which is well able to absorb full-size wave energy with periods in the range of 4s–7s. The simulation uses 1:10 scaling, so the radius R is 0.5 m, the total height is 0.6 m, and the wall thickness D of the air chamber is 0.01 m. The PTO damping is simulated by setting up an orifice above the air chamber [38], and the radius of the orifice is defined as R_o . The 3D model of the device is shown in Figure 3.

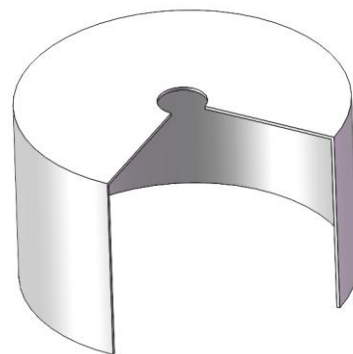


Figure 3. Three-dimensional model diagram of the OWC chamber primary structure.

A 3D numerical water flume for analyzing the performance of the OWC device is subsequently established. The positive direction of the x -axis is set as the direction of wave propagation, and the fifth-order Stokes wave is used to simulate the wave conditions. The OWC device is placed in a position 15 m away from the incident boundary. The wave generation and absorption zones are configured to eliminate the influence of wave reflection on the experimental results. The water depth h is 1 m, and the draft of the device d is 0.2 m. The overall schematic of the numerical model is shown in Figure 4. In instances where the width of the flume exceeds five times the width of the device, the impact of the flume wall on the experiment is rendered negligible [39]. Consequently, the width of the flume is designated to be 7 m. Three wave height detection points, G1 (0 m, 0 m), G2 (−0.25 m, 0 m), and G3 (0.25 m, 0 m), are established to detect the wave surface height inside the air chamber. Two pressure monitoring points, P1 (−0.25 m, 0.39 m) and P2 (0.49 m, 0.3m), are set at the inner wall and the top of the chamber to detect the air pressure inside the chamber. The average of the obtained values is taken as the overall pressure value.

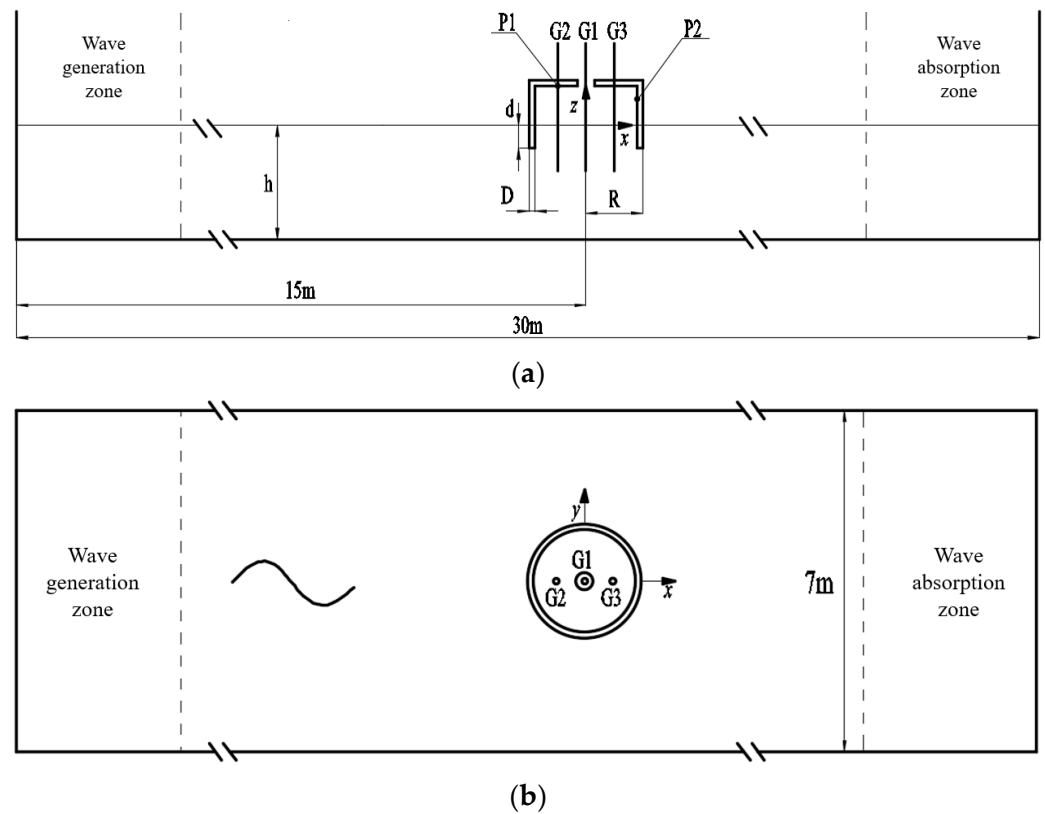


Figure 4. Sketch of the numerical water flume: (a) front view and (b) top view.

3.2. Numerical Modeling

Water and air are assumed to be incompressible, which is considered a valid assumption for devices at experimental scales [40]. The continuity of the two-phase (air and water) flow and the Navier–Stokes equations are used here as controlling equations [41]:

$$\nabla \cdot u = 0 \quad (1)$$

$$\frac{\partial u}{\partial t} + (u \cdot \nabla)u = -\frac{1}{\rho} \nabla p + \frac{\mu_e}{\rho} \nabla \cdot (\nabla u) + f \quad (2)$$

where $u = (u_x, u_y, u_z)$ denotes the fluid velocity, $\nabla = (\partial/\partial x, \partial/\partial y, \partial/\partial z)$ is the gradient operation, ρ is the fluid density, p is the pressure in excess of the hydrostatic pressure of the fluid, f is the volumetric force of gravity, and μ_e is the dynamic viscosity. The above equations are then further closed using the SST k - ω turbulence model, which is a turbulence model whose ability to capture better detailed flow field information, such as velocity, eddies with higher accuracy [42]. The transport equations of the model can be expressed as follows [43]:

$$\frac{\partial \rho k}{\partial t} + \frac{\partial \rho u_j k}{\partial x_j} = \frac{\partial}{\partial x_j} \left[(\mu_{lam} + \sigma_k \mu_{turb}) \frac{\partial k}{\partial x_j} \right] - \beta^* \rho \omega k + \tau_{ij} \frac{\partial u_i}{\partial x_j} \quad (3)$$

$$\begin{aligned} \frac{\partial \rho \omega}{\partial t} + \frac{\partial \rho u_j \omega}{\partial x_j} &= \frac{\partial}{\partial x_j} \left[(\mu_{lam} + \sigma_\omega \mu_{turb}) \frac{\partial \omega}{\partial x_j} \right] + \gamma \frac{\rho}{\mu_{turb}} \tau_{turb,ij} \frac{\partial u_i}{\partial x_j} \\ &- \beta \rho \omega^2 + 2(1 - F_\varphi) \frac{\rho \sigma_\omega}{\omega} \frac{\partial k}{\partial x_j} \frac{\partial \omega}{\partial x_j} \end{aligned} \quad (4)$$

where x_j is the position vector, u_j is the velocity vector, and μ_{lam} and μ_{turb} are the laminar and turbulent viscosities, respectively. τ_{turb} is the Favre-averaged Reynolds stress calculated according to the Boussinesq eddy viscosity assumption.

In order to better simulate and track the state of motion of the free surface, the volume of fluid (VOF) method [44] is used. The volume fraction of water within the computational cell satisfies the following advection equation:

$$\frac{\partial \phi}{\partial t} + \nabla \cdot (\phi u) + \nabla \cdot (\phi(1 - \phi)u_r) = 0 \quad (5)$$

where u_r indicates the relation of velocity between air and water. The phases of the computational grid are mainly determined by the volume fraction ϕ and are defined as follows: $\phi = 1$ corresponds to the water phase, $0 < \phi < 1$ represents the mixed air and water phase, and $\phi = 0$ indicates the air phase. Therefore, in the numerical simulation, the fluid density and dynamic viscosity can be expressed as follows:

$$\rho = \phi \rho_{water} + (1 - \phi) \rho_{air} \quad (6)$$

$$\mu = \phi \mu_{water} + (1 - \phi) \mu_{air} \quad (7)$$

Regarding the boundary conditions of the simulated wave flume, the upper boundary is designated as the pressure outlet. The bottom is designated as the wall boundary, and the wave generation and absorption boundaries are set as the velocity inlet boundary. The two flume sides are defined as symmetry plane boundary conditions. The wave generation and absorption zones are set as wave forcing zones, with their length set to 1.5 times the incident wave wavelength [45].

The entire numerical flume is meshed using the built-in automatic meshing technique in STARCCM+. The grid size setting is a critical factor in the process of numerical simulation which determines the efficiency of the numerical simulation. To accurately capture the wave motion and the output power of the air chamber, the mesh size in the vertical z -direction of the free surface region and the OWC opening region needs to be refined. Three mesh sizes, $15/H$, $20/H$, and $25/H$, were selected to analyze the mesh convergence. Figure 5 represents the variations in wave surface height and pressure inside the OWC device with time for different grid sizes (wave height $H = 0.2$ m, period $T = 1.8$ s).

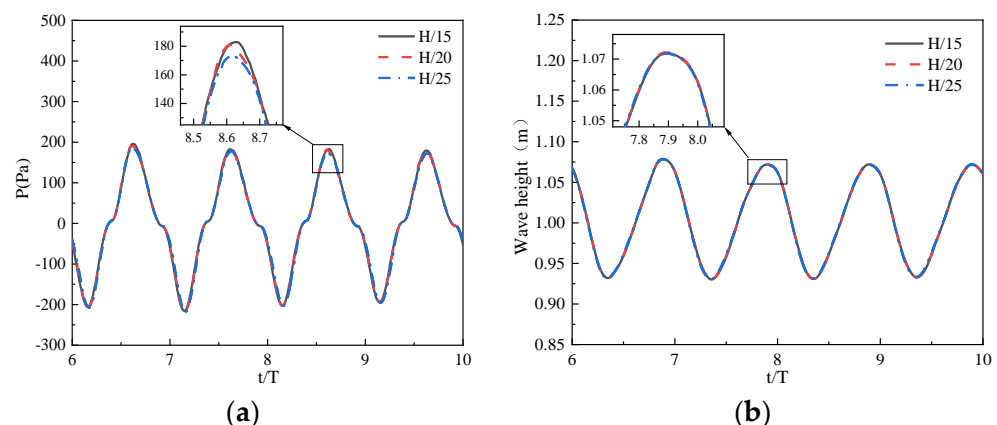


Figure 5. Comparison of simulation outcomes utilizing various mesh sizes: (a) pressure and (b) wave height.

It can be found that the variations in pressure and wave height values tend to be approximately the same for the three grid sizes. The pressure of the two sparser grids and the third grid differ by 3.2% and 2.5%, respectively, while the troughs differ by 2.23% and 1.1%. Similar conclusions can be drawn from the plots of wave height. Thus, with the above analysis, the grid can be considered to have converged, and the size of the

encrypted grid is set to $H/20$ in the following analysis. The overall grid delineation is shown in Figure 6.

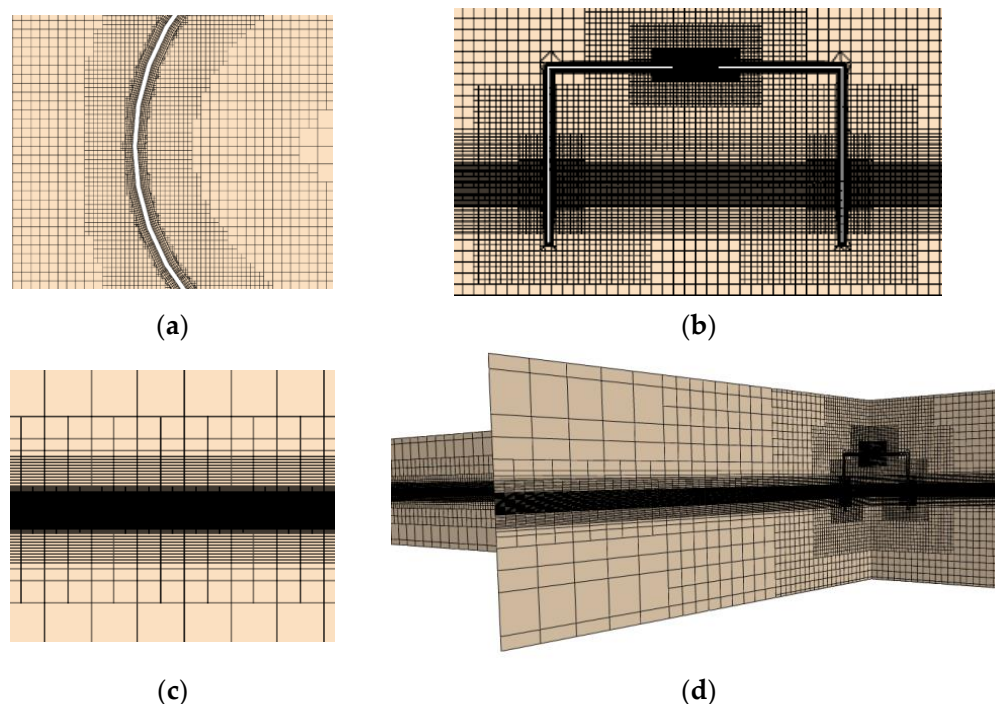


Figure 6. Mesh configuration for the numerical wave flume: (a) mesh distribution surrounding the structure (top–down view); (b) mesh distribution surrounding the structure (frontal view); (c) distribution of the mesh along the water depth direction; and (d) general overview of the mesh distribution.

3.3. Numerical Model Validation

To validate the dependability of the developed numerical model, the experimental results of the interaction model between waves and offshore fixed OWC devices conducted by Iturrioz et al. [46] were used for verification. The overall dimensions of the OWC device are shown in Figure 7, with a water depth of 0.6 m. The incident wave parameters were established with a wave height $H = 0.08$ m and period $T = 1.3$ s.

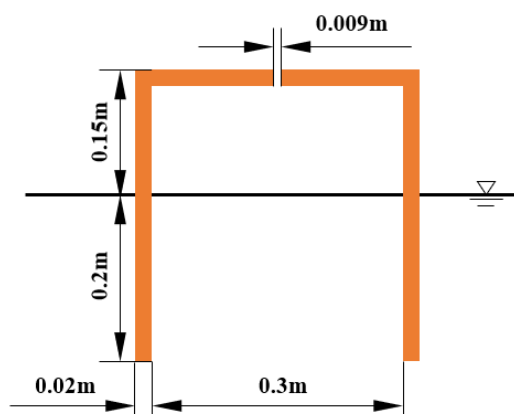


Figure 7. Overall dimensions of OWC device.

The wave height and air pressure inside the chamber obtained from the simulation are compared with those obtained from the model experiment, with the result shown in Figure 8. The trend of the two changes is consistent, and the degree of overlap is high.

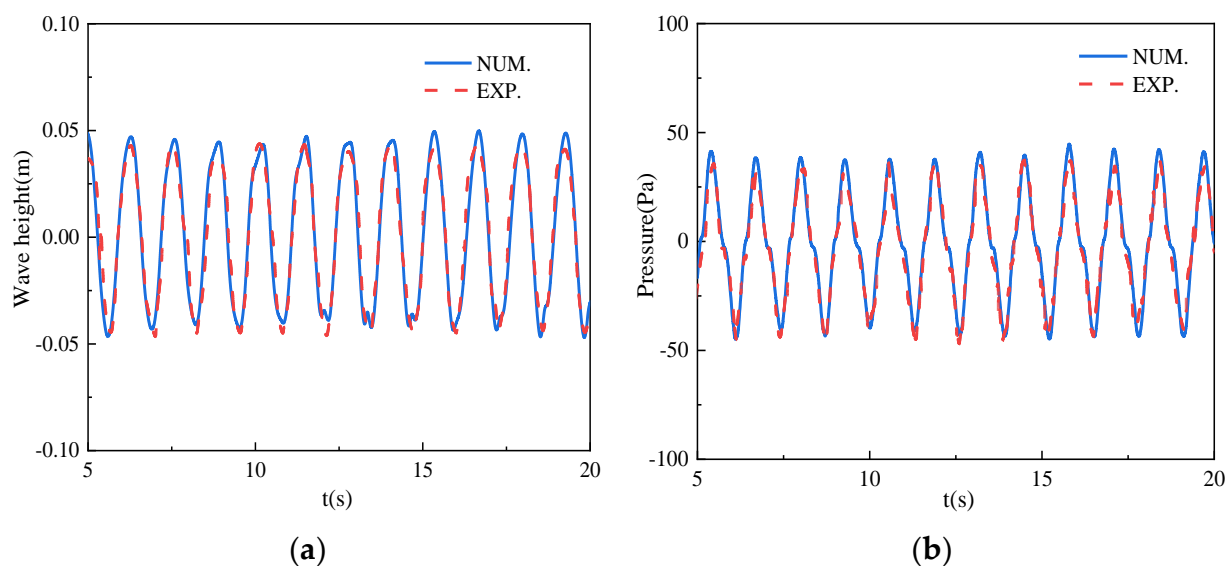


Figure 8. Comparison chart of simulation results and model experiment results: (a) wave height and (b) pressure.

4. Hydrodynamic Numerical Analysis and Discussion

In order to investigate the energy conversion mechanism in the hydrodynamic stage of the OWC device and further analyze the effects of the device's opening ratio on energy conversion under different wave conditions, the opening ratio is defined as $\varepsilon = S_o/S_w$, where S_o is the opening area of the device, while S_w is the total wave surface area within the air chamber. The opening ratio is typically selected within the range of 0.5% to 2% [47].

4.1. Analysis of Energy Conversion Process

As demonstrated in Figure 9, the airflow velocity in the OWC device during a wave cycle is illustrated, and the wave surface height in the device at its corresponding moment is shown in Figure 10. At the moment of $1/4 T$, the wave surface inside the air chamber moves upward, which squeezes the air within the chamber. At this moment, the air pressure reaches its maximum value of 183.23 Pa, corresponding to the maximum upward velocity of the wave surface. Simultaneously, the airflow velocity at the orifice also attains its highest value, with an average airflow velocity of 12.45 m/s. At the moment of $1/2 T$, the wave surface reaches its highest point of 0.065 m, at which point the air inside the chamber is no longer compressed. As a result, the airflow will change direction from flowing out of the chamber to entering the chamber, and the chamber pressure becomes 0 Pa. At the moment of $3/4 T$, the wave surface moves continuously downward, causing the device to take in air from the atmosphere constantly. The velocity of the wave surface reaches its maximum negative value, resulting in the air chamber pressure dropping to its minimum of -191.2 Pa, while the airflow velocity reaches its peak in the opposite direction, with an average airflow velocity of -12.86 m/s. Finally, at the moment of T , the wave surface reaches the lowest point -0.069 m, and the device no longer takes in air, which is the secondary reversal moment of airflow rate. The air chamber pressure also reaches 0 Pa. Subsequently, the wave surface continues to move upward, repeating this process. This cyclical motion constitutes the energy harvesting process of the OWC device.

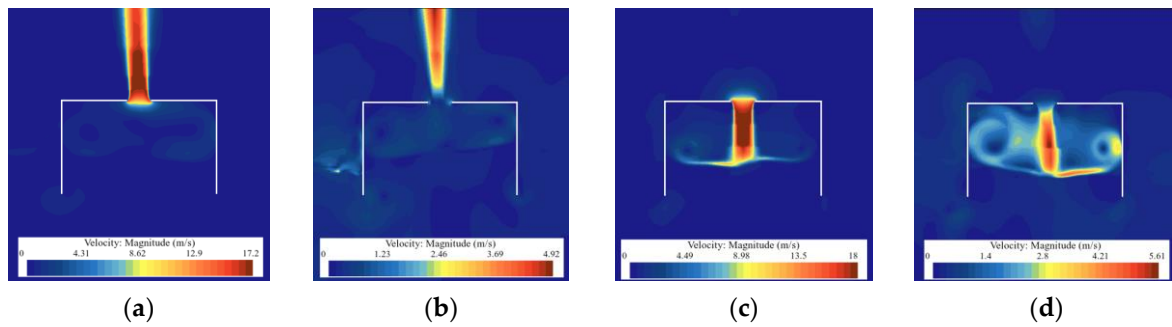


Figure 9. Airflow velocity in the OWC device during a wave cycle: (a) $1/4 T$; (b) $1/2 T$; (c) $3/4 T$; and (d) T . ($H = 0.2 \text{ m}$; $T = 1.5 \text{ s}$).

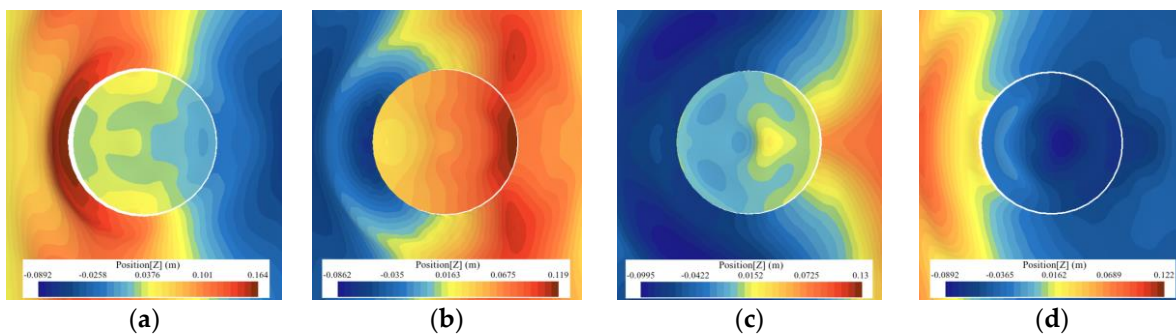


Figure 10. Wave surface height in the OWC device during a wave cycle: (a) $1/4 T$; (b) $1/2 T$; (c) $3/4 T$; and (d) T . ($H = 0.2 \text{ m}$; $T = 1.5 \text{ s}$).

In this paper, hydrodynamic efficiency is employed as a metric to assess the primary energy conversion efficiency of the OWC system, which can visually reflect the hydrodynamic performance of the device.

$$\xi = \frac{P_{air}}{P_w W} \tag{8}$$

where P_{air} is the energy absorbed by the OWC, P_w is the power unit width of the incident wave, and W represents the projected breadth of the OWC in the direction of the incident wave. In this paper, $W = 2R$. P_{air} and P_w can be calculated as follows.

$$P_{air} = \frac{1}{T} \int_{t_0}^{t_0+T} Q(t)P(t)dt \tag{9}$$

where T is the period of the incident wave, $Q(t)$ is the volume flow rate of the air through the orifice, and $P(t)$ is the relative air pressure in the chamber.

$$P_w = \frac{1}{2} \rho g A_i^2 c_g \tag{10}$$

where g is the gravitational acceleration, ρ is the water’s density, and A_i is the incident wave’s amplitude. The group velocity of the incident wave c_g can be defined as

$$c_g = \frac{c}{2} \left(1 + \frac{2kh}{\sinh 2kh} \right) \tag{11}$$

where k represents the wave number, and c is velocity of the incident wave which can be described as

$$c = \frac{\omega}{k} \tag{12}$$

To more accurately reflect the overall movement of the waves within the air chamber, wave heights measured simultaneously at detection points G1, G2, and G3 under different wave heights η_1 , η_2 , and η_3 are averaged to determine the wave surface elevation in the air chamber.

$$\eta = \frac{\eta_1 + \eta_2 + \eta_3}{3} \quad (13)$$

4.2. Effects of Incidence Wave Period

To study the hydrodynamic effects of different incident wave periods on the OWC device, the opening ratio was set as $\varepsilon = 2\%$, and the incident wave height was specified to be 0.2 m. The other parameters were set as follows: $h = 1$ m, $d = 0.2$ m, $R = 1$ m, and $D = 0.01$ m.

Figure 11 shows the wave height versus time inside the air chamber at different incidence wave periods, and the time is dimensionless for comparative analysis so that the horizontal coordinate is set as t/T . It is evident that the wave surface height in the air chamber varies approximately sinusoidally, with the amplitude of the crests exceeding that of the troughs. Furthermore, as the incident wave period increases, the maximum value of the wave height experiences a corresponding rise. The wave height can reach 1.1 m at $T = 2.4$ s, while the minimum is only 1.04 m at $T = 1.2$ s.

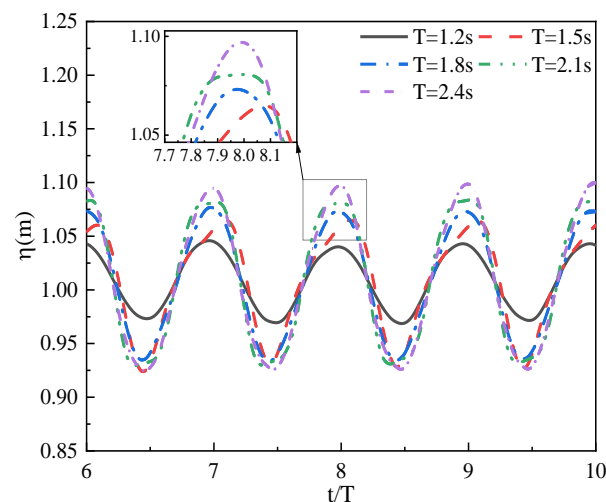


Figure 11. The wave height versus time inside the air chamber at various incident wave periods.

Figure 12 shows the air pressure versus time inside the air chamber at different incident wave periods. It can be observed that the maximum value of pressure exhibits an irregular variation with the increase in the incidence period. For $T = 1.5$ s and $T = 2.1$ s, the maximum pressure values are relatively close, at 193 Pa and 187 Pa, respectively, while for $T = 1.2$ s, the maximum pressure value is the smallest, at only 86 Pa.

The airflow velocity at the opening orifice and the captured power of the air chamber versus time for different incident periods are shown in Figures 13 and 14, respectively. It can be observed that the variation trends of the parameters under different periods are significantly different. Both the maximum airflow velocity and captured power are recorded at $T = 2.1$ s, with the maximum airflow velocity reaching 13.58 m/s and the captured power reaching 50.1 W. The minimum values are recorded at $T = 1.2$ s, with the airflow velocity and power only reaching 8.96 m/s and 13.97 W, respectively. Additionally, it can be noticed that there are some differences in the crest values of the airflow entering and exiting the chamber across the two stages. However, the differences between the two stages are relatively small at $T = 1.2$ s and $T = 1.5$ s. Figure 11 shows that the captured power of the OWC system is highly unstable, dropping to 0 W twice within each wave

period, which is mainly related to the characteristics of the wave itself. It is difficult to solve the unstable power output from the first stage of the energy conversion process.

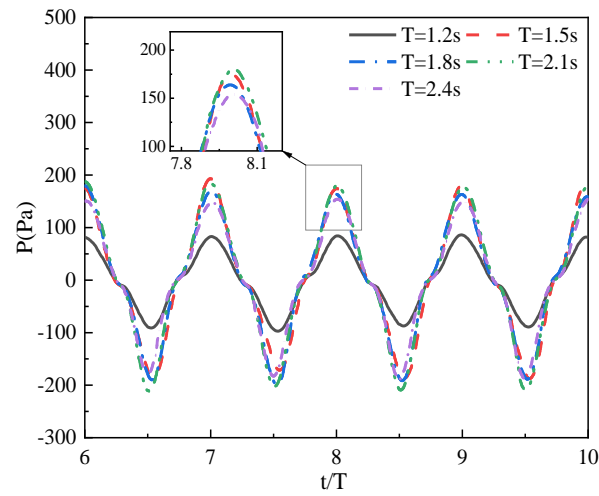


Figure 12. The air pressure versus time inside the air chamber at various incident wave periods.

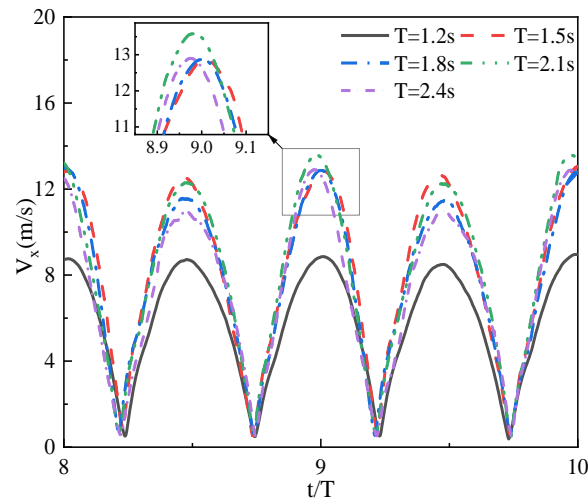


Figure 13. The airflow velocity at the opening orifice versus time at various incident wave periods.

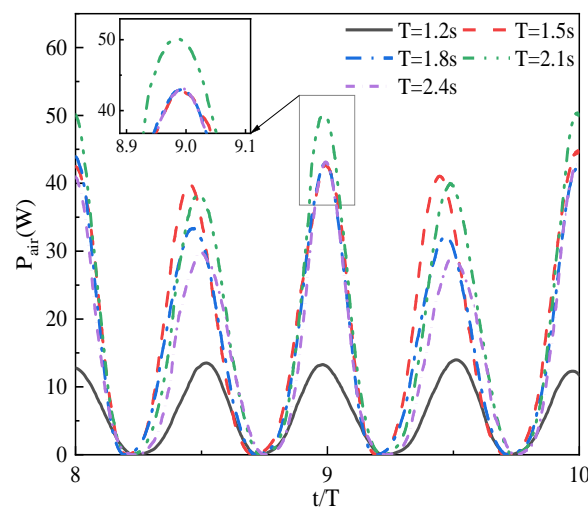


Figure 14. The captured power of air chamber versus time at various incident wave periods.

The numerical simulation results of the hydrodynamic efficiency of the OWC at different incident wave periods and the corresponding fitting line are shown in Figure 15. The figure demonstrates that hydrodynamic efficiency initially rises and subsequently declines with the period. The effective period bandwidth of the efficiency $\xi \geq 0.2$ is marked with a dashed line in the figure, and it can be found that the effective period bandwidth of the device is mainly in the range of 1.3 s to 2.1 s. The maximum hydrodynamic efficiency point was obtained at $T = 1.5$ s, reaching 0.322, from which it is inferred that the resonant period of the OWC occurs around $T = 1.5$ s. In contrast, the minimum point was obtained at $T = 3$ s, which was only 0.088. When the wave period is small, the reflection effect is strong, and most of the energy is reflected when it meets the front wall of the OWC and cannot enter the interior of the OWC, thus lowering the captured energy and hydrodynamic efficiency. When the wave period is large, the transmissivity of the waves will increase, and the waves will propagate directly through the OWC system, resulting in a decrease in the efficiency of the OWC system.

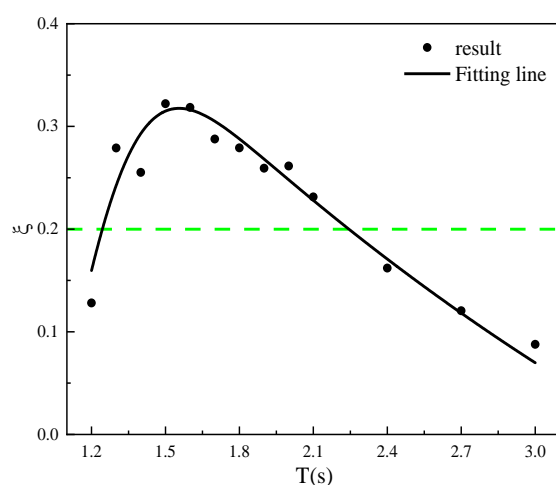


Figure 15. The hydrodynamic efficiency of the OWC at various incident wave periods.

4.3. Effects of Opening Ratio

In this section, in order to investigate the effect of different opening sizes on the hydrodynamic characteristics of the OWC, three opening ratios are set as 2%, 1.5%, and 1%, corresponding to opening radii of $R_{o1} = 0.075$ m, $R_{o2} = 0.06$ m, and $R_{o3} = 0.05$ m, respectively. The wave height is set as 0.2 m, and other setup parameters are kept constant. Figure 16 shows the variation in the average wave surface elevation $\Delta\eta = (\eta_{\text{crest}} - \eta_{\text{trough}})/2$ inside the chamber with the incident wave period for different opening ratios. Different opening ratios have a large impact on the hydrodynamic characteristics of the OWC device. As the opening ratio decreases, which means the damping keeps increasing, the average wave surface elevation inside the air chamber keeps decreasing, and the overall trend is the same. The minimum value is observed at an opening ratio of 1% and an incident wave period of 1.2 s. The average wave surface elevation ratio to the incident wave amplitude is 0.283. The maximum value is attained at $\varepsilon = 2\%$ and $T = 2.1$ s, reaching 0.9415. It is noticed that near the resonant period of the device, the oscillation of the water column inside the air chamber is more intense, and the average wave surface elevation changes more significantly. At the high-period region, the ratio of the average wave surface elevation to the incident wave amplitude gradually converges to 1 [48], which is mainly due to the long wave which can penetrate the OWC more easily.

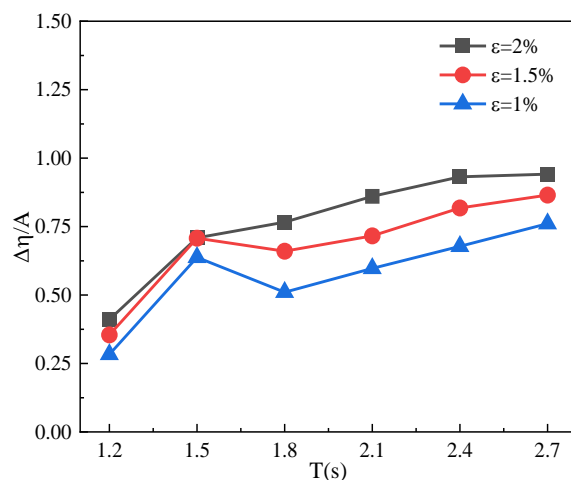


Figure 16. Variation in average wave surface elevation within the chamber with different incident wave periods at various opening ratios.

Figures 17 and 18 illustrate variation in the average pressure $\Delta P = (P_{crest} - P_{trough})/2$ inside the air chamber and the average airflow velocity at the opening orifice with the incident wave period for different opening ratios, respectively. It can be found that, under different opening ratios, the average pressure inside the air chamber and the average airflow velocity at the opening orifice show the same trend with the incident wave period. Both demonstrate an overall change process of increasing first and then decreasing, and both attain their maximum value at $T = 2.1$ s. As the opening ratio decreases, both pressure and air velocity increase, contrary to the tendency of the surface elevation inside the chamber. The pressure within the air chamber reaches 474.11 Pa and the average airflow velocity is 11.05 m/s at an opening ratio of 1% and a period of 2.1 s. Conversely, the minimum values are obtained at a 2% opening ratio with a 1.2 s period, which are 93.23 Pa and 5.27 m/s, respectively.

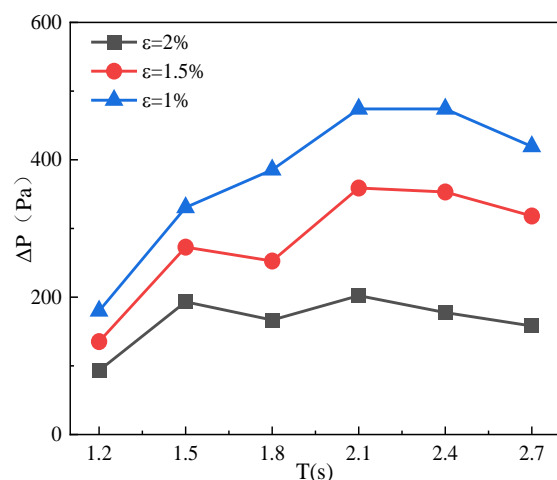


Figure 17. Variation in average pressure inside the chamber with different incident wave periods at various opening ratios.

The variation in hydrodynamic efficiency with the incident wave period for different opening ratios is shown in Figure 19. The overall trend of change is consistent. As the period increases, the hydrodynamic efficiency demonstrates a trend of an initial increase and subsequent decline. As the incident wave period of 1.5 s approaches the resonant period of the OWC device, the hydrodynamic efficiency is higher at the opening ratio of 2%, whereas smaller opening ratios ($\epsilon = 1.5\%$, $\epsilon = 1\%$) at high-period regions result in

higher efficiency. Consequently, in the face of different wave conditions, the PTO damping of the device should be appropriately selected. For instance, installing larger PTO damping in the high-period region can enhance the energy conversion efficiency of the first stage of the OWC device.

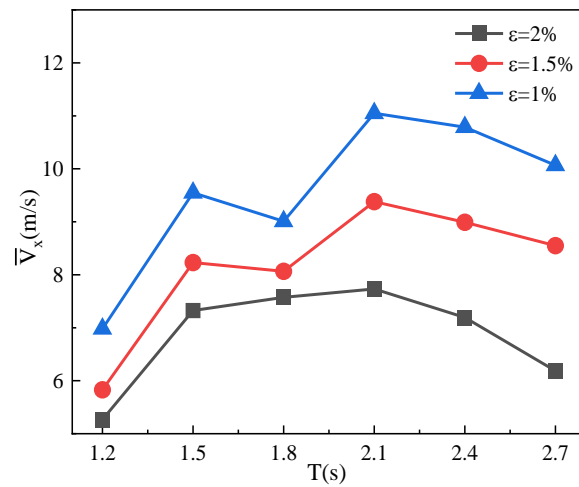


Figure 18. Variation in average airflow velocity at the opening orifice with different incident wave periods at various opening ratios.

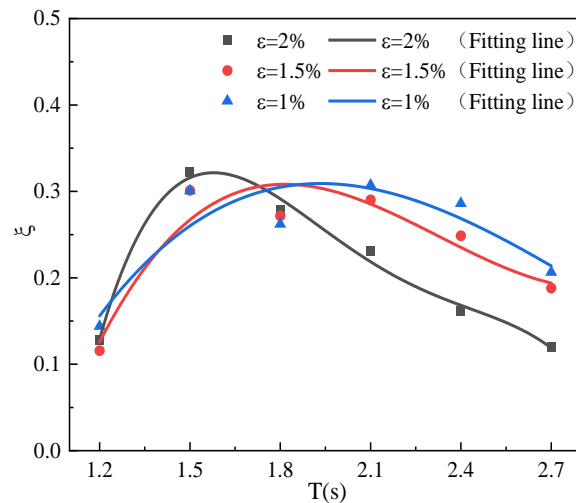


Figure 19. Variation in hydrodynamic efficiency of OWC with different incident wave periods at various opening ratios.

4.4. Effects of Incidence Wave Height

This section investigates the effects of different incident wave heights on the hydrodynamic efficiency of the OWC device. The opening ratio is 1.5%, and five wave height cases are selected ($H = 0.05$ m, 0.1 m, 0.15 m, 0.2 m, 0.25 m). All other variables remain unchanged. Figure 20 illustrates the relationship between hydrodynamic efficiency and incident wave height. It can be noticed that the overall hydrodynamic efficiency initially increases with the rise in incident wave height, attains a maximum value at the critical wave height H_i , and subsequently diminishes with an increase in wave height. The critical wave heights are not exactly the same across different incident wave periods, and the maximum efficiency values reach 0.33 and 0.31 at $T = 1.5$ s and $T = 2.1$ s when H_i is taken at 0.15 m, respectively. At $T = 1.8$ s, H_i is obtained at 0.1 m, and the maximum efficiency value is 0.29.

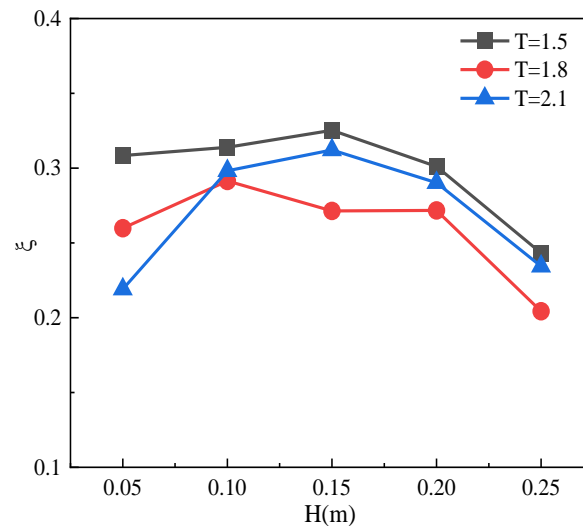


Figure 20. The variation in hydrodynamic efficiency with incident wave height.

5. Pneumatic System Simulation Analysis

5.1. Mathematical Problem

This paper assumes that air is an ideal gas. The following expression for the gas multivariable equation is satisfied for a given mass of gas.

$$p_1 V_1^n = p_2 V_2^n = C \quad (14)$$

where V_1 , p_1 , and V_2 , p_2 are the volume and pressure of the gas in the two equilibrium phases, respectively. n is the multivariate index, and different values of n correspond to different processes of change in gas.

Pneumatic check valves allow the gas passage in one direction while completely shutting off the gas in the other direction. The effective opening area and opening pressure are pivotal parameters that influence the operational efficiency of the equipment. The air mass flow rate through the check valve can be determined by steady-state subsonic flow modeling as

$$Q_v = C_v \alpha A_v \sqrt{2 \rho_{air} (p_{in} - p_{out})} \quad (15)$$

where C_v is the valve's discharge coefficient, αA_v is the effective opening area when the valve is fully open, ρ_{air} is the density of water, and p_{in} and p_{out} are the gas pressure at both ends of the check valve.

This paper utilizes a spring-loaded accumulator, which exhibits an optimal motion response. Assuming that the working motion of the accumulator is a solely axial motion, the volume of the accumulator storage chamber V_b can be expressed as

$$V_b = V_0 + A_a x(t) \quad (16)$$

where V_0 is the initial volume of the storage chamber, A_a is the piston area, and $x(t)$ is the piston displacement. Accordingly, the kinetic equations are established by Newton's second law.

$$m_a \ddot{x}(t) = (p_b - p_a) A_a - k_a x(t) - C_a \dot{x}(t) \quad (17)$$

where m_a is the mass of the piston, and p_a and p_b are the pressure at the spring section of the accumulator and the pressure in the gas storage chamber. The spring section is connected to the atmosphere, so the pressure is atmospheric pressure, and k_a and C_a are the spring stiffness and damping at the spring section. The flow rate is defined into the accumulator as q_b .

$$q_b = \dot{V}_b = A_a \dot{x}(t) \quad (18)$$

In the turbine module, a simplified analysis analogous to the check valve modeling is employed. In this analysis, the turbine is replaced by a small orifice, and its mass flow rate exhibits a quadratic relationship with the pressure drop.

$$Q_t = \sqrt{\frac{p_{up} - p_{down}}{k_t}} \quad (19)$$

where p_{up} and p_{down} are the pressure up- and downstream of the turbine, respectively; Q_t is the mass flow rate via the turbine; and k_t is the flow coefficient of the turbine, which is given as

$$k_t = \left(2\rho_{air}A_t^2C_t^2\right)^{-1} \quad (20)$$

where A_T is the orifice area and C_t is the discharge coefficient, which usually takes values between 0.5 and 1.

Finally, the output power of the turbine can be defined.

$$P_o = \frac{(P_{up} - P_{down})Q_t}{\rho_{air}} \quad (21)$$

5.2. Model Construction

The simulation model of the novel PTO system depicted in Figure 21 was constructed using AMESim (Version: 2020.1). The parameter input module mainly inputs the parameters of air chamber temperature (K) and air chamber pressure (barA) over time, which can be obtained from the hydrodynamic simulation analysis in the previous section, to the whole pneumatic system. The rectification circuit module mainly uses the check valve group to rectify the airflow into a unidirectional flow. The specific parameters and modeling of unidirectional turbines are not studied. Consequently, the orifice is utilized to replicate the dampening effect of the turbine, and the pneumatic power output is used to express the effect of energy conversion. In the accumulator module, a pneumatic accumulator model was constructed using components from the Pneumatic Component Design Library and the 1D Mechanical Library. A logic control loop uses signaling elements to control the switching valve under predetermined conditions, modulating the accumulator's charging and discharging states. This enhances the stability of the airflow through the turbine.

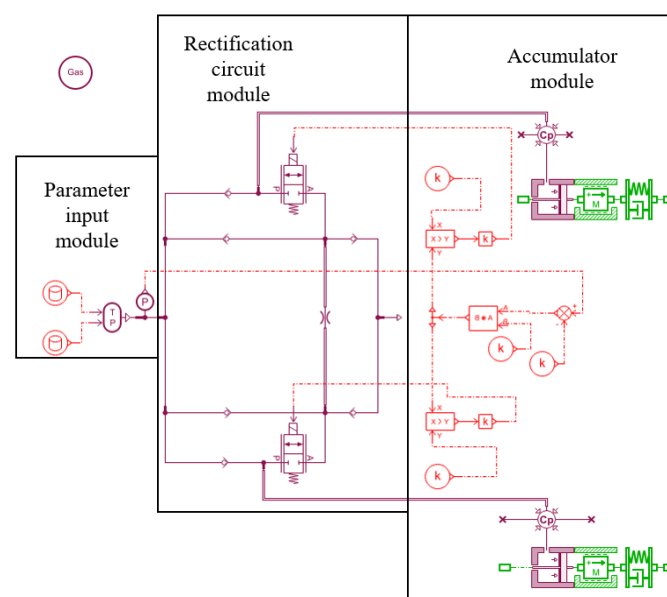


Figure 21. Simulation model of the novel PTO system.

5.3. Data Analysis

The pressure and temperature inside the air chamber were selected as inputs to the PTO system for $H = 0.2$ m and $T = 1.5$ s, $\varepsilon = 2\%$. The inputs to the PTO system after the air chamber operation has stabilized are shown in Figure 22.

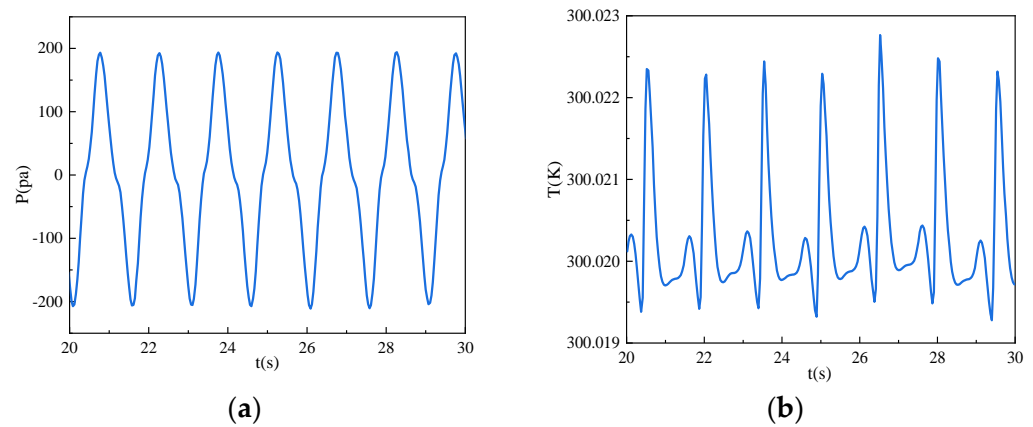


Figure 22. PTO system input values: (a) pressure and (b) temperature.

Assuming that the check valve and switching valve are either completely open or completely closed and there is no pressure loss, the positive pressure accumulator's initial volume is set as 0.5 L, while the negative pressure accumulator's initial volume is set as 10 L due to the need to form negative pressure. To investigate the impact of the accumulator on the system's energy conversion, a model of the rectifier loop PTO system without accumulators is constructed, as illustrated in Figure 23. This model will henceforth be referred to as the conventional PTO system.

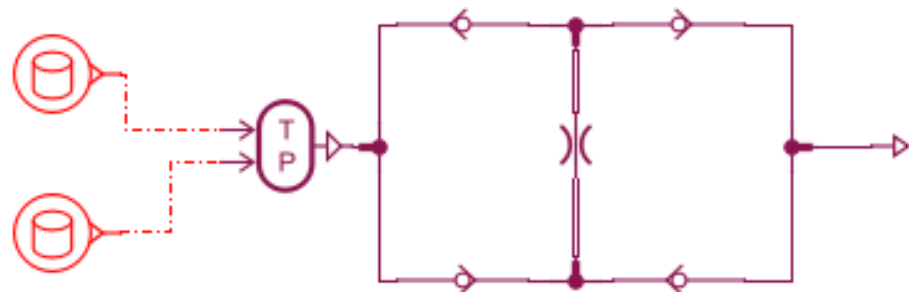


Figure 23. Simulation model of the conventional PTO system.

Figure 24 shows the mass flow rate via the turbine, and it can be found that the fluctuation of the flow rate via the turbine can be effectively reduced by setting the accumulator module. Figure 25 shows the pressure up- and downstream of the turbine in the novel PTO system compared to the conventional PTO system. In the conventional PTO system, it can be observed from the figure that, since the air chamber pressure reaches 0 Pa twice in a wave cycle, the pressure up- and downstream is equal, and no flow passes through. The accumulator system can effectively improve this phenomenon; when the air chamber pressure is close to 0 Pa, the switching valve opens so that the accumulator will release energy. This effectively prevents the pressure between the pressure up- and downstream of the turbine is equal.

Figure 26 compares the system's output power, and it can be more intuitively found that the addition of the accumulator leads to a more stable output power of the system.

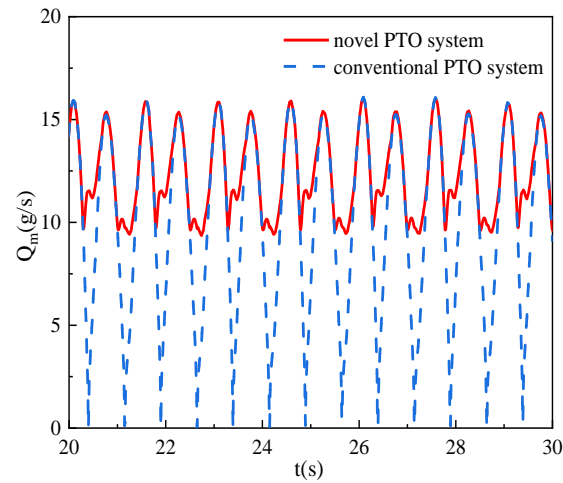


Figure 24. Comparison of mass flow rate via the turbine.

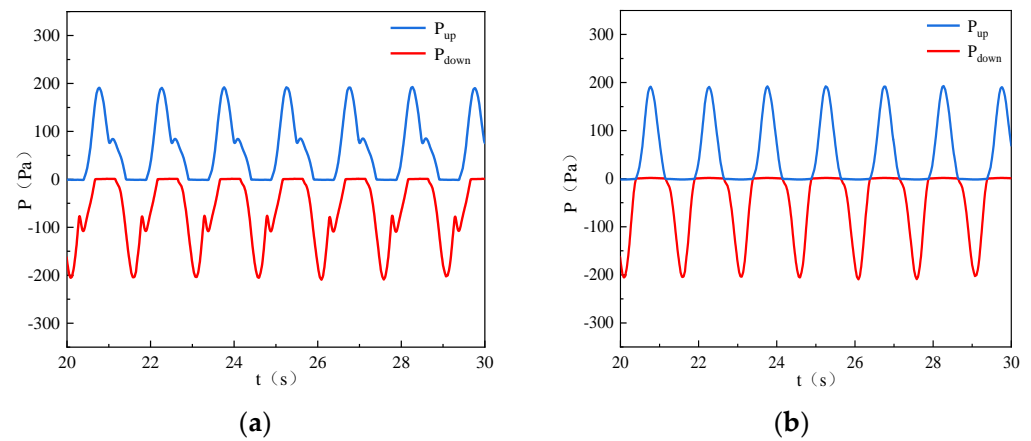


Figure 25. The pressure up- and downstream of the turbine: (a) novel PTO system and (b) conventional PTO system.

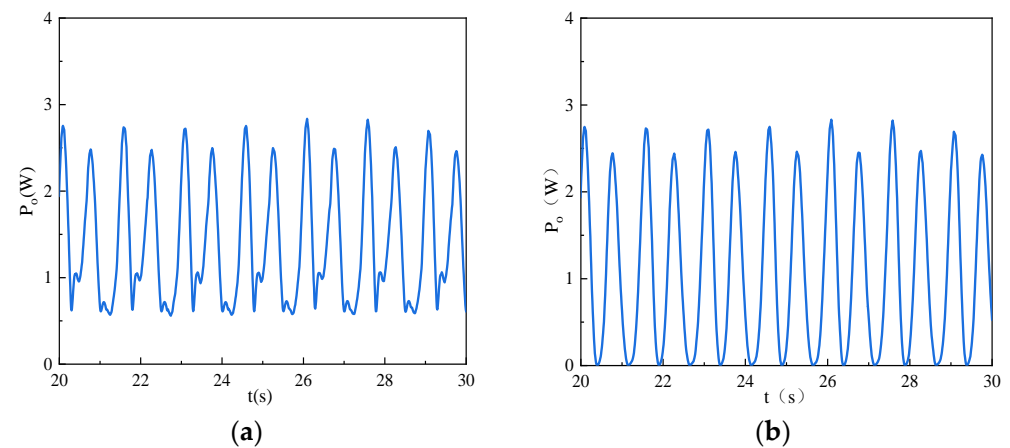


Figure 26. Comparison of the system's output power: (a) novel PTO system and (b) conventional PTO system.

The hydrodynamic outputs for $T = 1.8$ s and $T = 2.1$ s under identical parameters are subsequently applied to the PTO system using the same method. The results, presented in Figure 27, demonstrate that the novel PTO significantly enhances the stability of energy conversion under varying wave conditions.

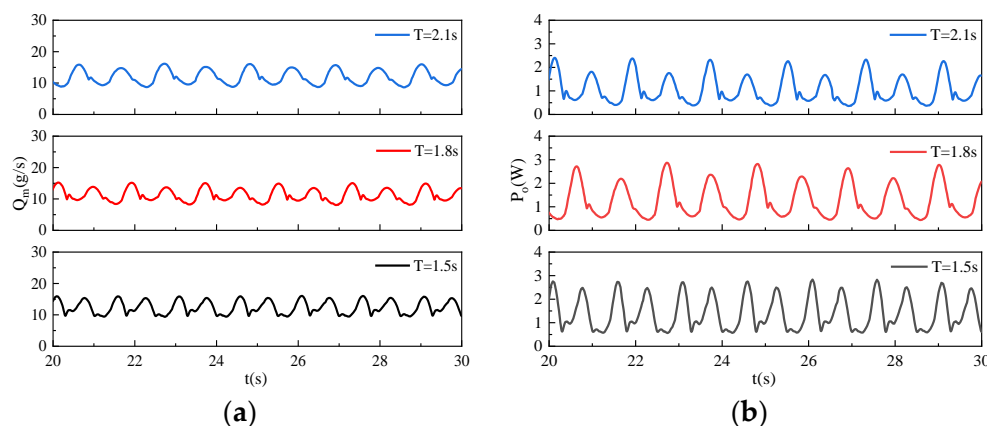


Figure 27. Novel PTO system for different input conditions: (a) mass flow rate and (b) output power.

6. Conclusions

In this paper, a novel OWC wave energy harvesting system constructed on the working principle of energy storage valve control, and the hydrodynamic performance of the OWC and the performance of the novel PTO system are studied. A 3D numerical simulation model of the OWC device was constructed using CFD software. The effects of incident wave period, wave height, and opening ratio on the hydrodynamic performance of the device were investigated. Subsequently, based on the analytical results, the designed novel PTO system was modeled using AMESim to explore the accumulator's effect on the overall device's stability for energy conversion. The final results are as follows:

- (1) As the period increases, the energy acquisition efficiency of the OWC device first rises, peaks at 1.5 s, and then declines. This is primarily because the device's resonant period is near 1.5 s, resulting in water column resonance within the air chamber and enhanced hydrodynamic performance. At shorter periods, stronger wave reflection reduces energy capture, while at longer periods, greater transmission limits energy absorption, resulting in suboptimal performance.
- (2) The opening ratio significantly affects the hydrodynamic efficiency of the OWC device. As the opening ratio decreases, the average wave surface elevation inside the chamber drops, while the average chamber pressure and airflow velocity at the orifice increase. The optimal opening ratio varies with the incident wave period. Increasing turbine damping in long-period wave conditions can enhance the energy conversion efficiency.
- (3) The height of the incident wave slightly affects the device's resonance period and hydrodynamic efficiency. The hydrodynamic efficiency initially increases and then decreases with rising wave height. The optimal wave height varies for different wave periods.
- (4) The novel PTO system, incorporating accumulators and switching valves, significantly improves airflow stability through the turbine, resulting in a more stable relative power output. The rational selection of the accumulator system parameters and the construction of the logic control of the switching valve can reduce the volatility of the mass flow rate via the turbine by 53.49% and the volatility of the output power by 25.46%.

Author Contributions: Conceptualization, software, methodology, data curation, and writing—original draft, Y.H.; conceptualization, investigation, and validation, Z.Y.; validation and writing—review and editing, C.W.; supervision, reviewing, and funding acquisition, Y.L.; supervision and editing, G.X. All authors contributed to the design of the study. All authors have read and agreed to the published version of the manuscript.

Funding: This research was funded by the National Natural Science Foundation of China, (U22A20242, 52171265, 52471331) and the National Key Research and Development Program of China (2023YFB4204103).

Data Availability Statement: The original contributions presented in the study are included in the article, and further inquiries can be directed to the corresponding authors.

Conflicts of Interest: The authors declare no conflicts of interest.

References

1. Alam, M.; Kayes, I.; Hasan, A.; Shahriar, T.; Habib, M.A. Exploring SAARC's Ocean Energy Potential: Current Status and Future Policies. *Energy Rep.* **2024**, *11*, 754–778. [[CrossRef](#)]
2. Cai, Q.; Zhu, S. Applying Double-Mass Pendulum Oscillator with Tunable Ultra-Low Frequency in Wave Energy Converters. *Appl. Energy* **2021**, *298*, 117228. [[CrossRef](#)]
3. Lopez, I.; Andreu, J.; Ceballos, S.; Martinez de Alegria, I.; Kortabarria, I. Review of Wave Energy Technologies and the Necessary Power-Equipment. *Renew. Sust. Energ. Rev.* **2013**, *27*, 413–434. [[CrossRef](#)]
4. Qiao, D.; Haider, R.; Yan, J.; Ning, D.; Li, B. Review of Wave Energy Converter and Design of Mooring System. *Sustainability* **2020**, *12*, 8251. [[CrossRef](#)]
5. Aderinto, T.; Li, H. Review on Power Performance and Efficiency of Wave Energy Converters. *Energies* **2019**, *12*, 4329. [[CrossRef](#)]
6. Handoko, C.R.; Mukhtasor. The Development of Power Take-off Technology in Wave Energy Converter Systems: A Review. *IOP Conf. Ser. Earth Environ. Sci.* **2021**, *739*, 012081. [[CrossRef](#)]
7. Delauré, Y.M.C.; Lewis, A. 3D Hydrodynamic Modelling of Fixed Oscillating Water Column Wave Power Plant by a Boundary Element Methods. *Ocean Eng.* **2003**, *30*, 309–330. [[CrossRef](#)]
8. Evans, D.V.; Porter, R. Hydrodynamic Characteristics of an Oscillating Water Column Device. *Appl. Ocean Res.* **1995**, *17*, 155–164. [[CrossRef](#)]
9. Falcao, A.F.O.; Henriques, J.C.C. The Spring-like Air Compressibility Effect in Oscillating- Water-Column Wave Energy Converters: Review and Analyses. *Renew. Sust. Energ. Rev.* **2019**, *112*, 483–498. [[CrossRef](#)]
10. Falcao, A.F.O.; Henriques, J.C.C. Oscillating-Water-Column Wave Energy Converters and Air Turbines: A Review. *Renew. Energy* **2016**, *85*, 1391–1424. [[CrossRef](#)]
11. Heath, T.V. A Review of Oscillating Water Columns. *Philos. Trans. R. Soc. A-Math. Phys. Eng. Sci.* **2012**, *370*, 235–245. [[CrossRef](#)]
12. Josset, C.; Clement, A.H. A Time-Domain Numerical Simulator for Oscillating Water Column Wave Power Plants. *Renew. Energy* **2007**, *32*, 1379–1402. [[CrossRef](#)]
13. Nagata, S.; Toyota, K.; Imai, Y.; Setoguchi, T.; Nakagawa, H. Frequency Domain Analysis on Primary Conversion Efficiency of a Floating OWC-Type Wave Energy Converter. Part1, Two Dimensional Problems. *J. Jpn. Soc. Nav. Archit. Ocean Eng.* **2011**, *14*, 123–133.
14. Iturrioz, A.; Guanche, R.; Armesto, J.A.; Alves, M.A.; Vidal, C.; Losada, I.J. Time-Domain Modeling of a Fixed Detached Oscillating Water Column towards a Floating Multi-Chamber Device. *Ocean Eng.* **2014**, *76*, 65–74. [[CrossRef](#)]
15. Mavrakos, S.A.; Konispoliatis, D.N. Hydrodynamics of a Free Floating Vertical Axisymmetric Oscillating Water Column Device. *J. Appl. Math.* **2012**, 142850. [[CrossRef](#)]
16. Ning, D.; Zhou, Y.; Zhang, C. Hydrodynamic Modeling of a Novel Dual-Chamber OWC Wave Energy Converter. *Appl. Ocean Res.* **2018**, *78*, 180–191. [[CrossRef](#)]
17. Ning, D.; Wang, R.; Zhang, C. Numerical Simulation of a Dual-Chamber Oscillating Water Column Wave Energy Converter. *Sustainability* **2017**, *9*, 1599. [[CrossRef](#)]
18. Konispoliatis, D.N. Hydrodynamic Analysis of a Dual Chamber Floating Oscillating Water Column Device. *Appl. Ocean Res.* **2025**, *154*, 104340. [[CrossRef](#)]
19. Ning, D.-Z.; Wang, R.-Q.; Zou, Q.-P.; Teng, B. An Experimental Investigation of Hydrodynamics of a Fixed OWC Wave Energy Converter. *Appl. Energy* **2016**, *168*, 636–648. [[CrossRef](#)]
20. Ning, D.; Wang, R.; Chen, L.; Sun, K. Experimental Investigation of a Land-Based Dual-Chamber OWC Wave Energy Converter. *Renew. Sust. Energ. Rev.* **2019**, *105*, 48–60. [[CrossRef](#)]
21. Lopez, I.; Carballo, R.; Taveira-Pinto, F.; Iglesias, G. Sensitivity of OWC Performance to Air Compressibility. *Renew. Energy* **2020**, *145*, 1334–1347. [[CrossRef](#)]
22. Liu, Z.; Xu, C.; Qu, N.; Cui, Y.; Kim, K. Overall Performance Evaluation of a Model-Scale OWC Wave Energy Converter. *Renew. Energy* **2020**, *149*, 1325–1338. [[CrossRef](#)]
23. Zhou, Y.; Ning, D.; Liang, D.; Cai, S. Nonlinear Hydrodynamic Analysis of an Offshore Oscillating Water Column Wave Energy Converter. *Renew. Sust. Energ. Rev.* **2021**, *145*, 111086. [[CrossRef](#)]

24. Joensen, B.; Bingham, H.B.; Read, R.W.; Nielsen, K.; Trevino, J.B. Hydrodynamic Analysis of One-Way Energy Capture by an Oscillating Water Column Wave Energy Device. *Energy Rep.* **2023**, *9*, 5306–5322. [[CrossRef](#)]
25. Gao, J.; Mi, C.; Song, Z.; Liu, Y. Transient Gap Resonance between Two Closely-Spaced Boxes Triggered by Nonlinear Focused Wave Groups. *Ocean Eng.* **2024**, *305*, 117938. [[CrossRef](#)]
26. Gong, S.; Gao, J.; Song, Z.; Shi, H.; Liu, Y. Hydrodynamics of Fluid Resonance in a Narrow Gap between Two Boxes with Different Breadths. *Ocean Eng.* **2024**, *311*, 118986. [[CrossRef](#)]
27. Mi, C.; Gao, J.; Song, Z.; Liu, Y. Hydrodynamic Wave Forces on Two Side-by-Side Barges Subjected to Nonlinear Focused Wave Groups. *Ocean Eng.* **2025**, *317*, 120056. [[CrossRef](#)]
28. Liu, Z.; Xu, C.; Kim, K. A CFD-Based Wave-to-Wire Model for the Oscillating Water Column Wave Energy Converter. *Ocean Eng.* **2022**, *248*, 110842. [[CrossRef](#)]
29. Yang, C.; Xu, T.; Wan, C.; Liu, H.; Su, Z.; Zhao, L.; Chen, H.; Johanning, L. Numerical Investigation of a Dual Cylindrical OWC Hybrid System Incorporated into a Fixed Caisson Breakwater. *Energy* **2023**, *263*, 126132. [[CrossRef](#)]
30. Zeng, Y.; Shi, W.; Michailides, C.; Ren, Z.; Li, X. Turbulence Model Effects on the Hydrodynamic Response of an Oscillating Water Column (OWC) with Use of a Computational Fluid Dynamics Model. *Energy* **2022**, *261*, 124926. [[CrossRef](#)]
31. Fan, Q.; Zhan, J.; Hu, W.; Huang, Z. Effects of Orifice Size on the Efficiency of a Heaving Oscillating Water Column. *Eng. Appl. Comp. Fluid Mech.* **2022**, *16*, 676. [[CrossRef](#)]
32. Peng, J.; Hu, C.; Yang, C. Influence of Incoming Wave Conditions on the Hysteretic Behavior of an Oscillating Water Column System for Wave Energy Conversion. *Ocean Eng.* **2023**, *280*, 114828. [[CrossRef](#)]
33. Xie, G.; Zhao, T.; Ma, Y.; Ni, W.; Hu, C. Investigation on the Wave Focusing Effects and Energy Capture of Oscillating Water Column Array. *Renew. Energy* **2025**, *238*, 121901. [[CrossRef](#)]
34. Vicente, M.; Benreguig, P.; Crowley, S.; Murphy, J. Tupperwave-preliminary numerical modelling of a floating OWC equipped with a unidirectional turbine. In Proceedings of the 12th European Wave and Tidal Energy Conference (EWTEC), Cork, Ireland, 27 August–1 September 2017.
35. Jayashankar, V.; Anand, S.; Geetha, T.; Santhakumar, S.; Kumar, V.J.; Ravindran, M.; Setoguchi, T.; Takao, M.; Toyota, K.; Nagata, S. A Twin Unidirectional Impulse Turbine Topology for OWC Based Wave Energy Plants. *Renew. Energy* **2009**, *34*, 692–698. [[CrossRef](#)]
36. Martinelli, L.; Ruol, P.; Fassina, E.; Giuliani, F.; Delmonte, N. A Wave-2-Wire Experimental Investigation of the New “Seabreath” Wave Energy Converter: The Hydraulic Response. *Coast. Eng. Proc.* **2014**, *1*, 29. [[CrossRef](#)]
37. Benreguig, P.; Vicente, M.; Dunne, A.; Murphy, J. Modelling Approaches of a Closed-Circuit OWC Wave Energy Converter. *J. Mar. Sci. Eng.* **2019**, *7*, 23. [[CrossRef](#)]
38. Ning, D.; Zhou, Y.; Mayon, R.; Johanning, L. Experimental Investigation on the Hydrodynamic Performance of a Cylindrical Dual-Chamber Oscillating Water Column Device. *Appl. Energy* **2020**, *260*, 114252. [[CrossRef](#)]
39. Soares, C.G. Offshore Structure Modelling. *Appl. Ocean Res.* **1995**, *17*, 391–392. [[CrossRef](#)]
40. Sarmiento, A.; Falcao, A. Wave Generation by an Oscillating Surface-Pressure and Its Application in Wave-Energy Extraction. *J. Fluid Mech.* **1985**, *150*, 467–485. [[CrossRef](#)]
41. Song, Z.; Jiao, Z.; Gao, J.; Mi, C.; Liu, Y. Numerical Investigation on the Hydrodynamic Wave Forces on the Three Barges in Proximity. *Ocean Eng.* **2025**, *316*, 119941. [[CrossRef](#)]
42. Elhanafi, A.; Fleming, A.; Macfarlane, G.; Leong, Z. Numerical Energy Balance Analysis for an Onshore Oscillating Water Column-Wave Energy Converter. *Energy* **2016**, *116*, 539–557. [[CrossRef](#)]
43. Tian, S.; Wu, L. Multiscale Modelling and Simulation of Coexisting Turbulent and Rarefied Gas Flows. *J. Fluid Mech.* **2024**, *1002*, A10. [[CrossRef](#)]
44. Hirt, C.; Nichols, B. Volume of Fluid (Vof) Method for the Dynamics of Free Boundaries. *J. Comput. Phys.* **1981**, *39*, 201–225. [[CrossRef](#)]
45. Fu, L.; Cheng, Y. Hydrodynamic Performance of a Dual-Floater Integrated System Combining Hybrid WECs and Floating Breakwaters. *China Ocean Eng.* **2022**, *36*, 969–979. [[CrossRef](#)]
46. Iturrioz, A.; Guanache, R.; Lara, J.L.; Vidal, C.; Losada, I.J. Validation of OpenFOAM[®] for Oscillating Water Column Three-Dimensional Modeling. *Ocean Eng.* **2015**, *107*, 222–236. [[CrossRef](#)]
47. Kharkeshi, B.A.; Shafaghat, R.; Jahanian, O.; Alamian, R.; Rezanejad, K. Experimental Study of an Oscillating Water Column Converter to Optimize Nonlinear PTO Using Genetic Algorithm. *Energy* **2022**, *260*, 124925. [[CrossRef](#)]
48. Zhou, Y.; Zhang, C.; Ning, D. Hydrodynamic Investigation of a Concentric Cylindrical OWC Wave Energy Converter. *Energies* **2018**, *11*, 985. [[CrossRef](#)]

Disclaimer/Publisher’s Note: The statements, opinions and data contained in all publications are solely those of the individual author(s) and contributor(s) and not of MDPI and/or the editor(s). MDPI and/or the editor(s) disclaim responsibility for any injury to people or property resulting from any ideas, methods, instructions or products referred to in the content.